crystals

MDPI

Article

Enhanced Mechanical and Thermal Properties of Waste Electric Porcelain-Based Solar Energy-Absorbing Thermal Storage Ceramics with Interwoven Mullite Structure

Xuejia Zhang [1], Zhenfei Lv [1,2,3,4,*], Junchi Weng [1], Mengke Fan [1], Feiyu Fan [1], Xin Wang [1], Xuyi Chen [1], Siqi Shi [1] and Xiulin Shen [1,2,3,4,*]

[1] School of Materials Science and Engineering, Anhui University of Science and Technology, Huainan 232001, China; xuejiazhang@aust.edu.cn (X.Z.); 2024201050@aust.edu.cn (J.W.); fmk@aust.edu.cn (M.F.); 2021303269@aust.edu.cn (F.F.); wx@aust.edu.cn (X.W.); 2022303434@aust.edu.cn (X.C.)
[2] Key Laboratory of Industrial Dust Prevention and Control & Occupational Health and Safety, Ministry of Education, Anhui University of Science and Technology, Huainan 232001, China
[3] Anhui Industrial Generic Technology Research Center for New Materials from Coal-Based Solid Wastes, Huainan 232001, China
[4] Anhui International Joint Research Center for Nano Carbon-Based Materials and Environmental Health, Huainan 232001, China
* Correspondence: zflv@aust.edu.cn (Z.L.); xlshen@aust.edu.cn (X.S.)

Abstract: This study addresses the environmental and resource challenges posed by the growing volume of waste electric porcelain in the power industry by developing solar absorption and thermal storage integrated ceramics (SATS ceramics) from waste electric porcelain. These SATS ceramics, which feature an exceptional mullite structure, were crafted through the optimization of the sintering process. Notably, when sintered at 1400 °C with an 11 wt.% magnetite content, the resulting material boasts an optimal short-clustered, ordered, and interwoven columnar mullite structure. This structure endows the material with a remarkable flexural strength of 96.05 MPa and a specific heat capacity of up to 0.6415 J/(g* °C) at 300 °C, significantly enhancing its thermal energy storage efficiency. This research offers innovative insights into the high-value utilization of waste electric porcelain and the development of solar thermal storage materials, underscoring its significant environmental and economic advantages.

Keywords: waste electric porcelain; solar energy storage; magnetite; mullite phase; material properties

Academic Editors: Andrzej Kruk and Dorota Sitko

Received: 23 December 2024
Revised: 11 January 2025
Accepted: 16 January 2025
Published: 18 January 2025

Citation: Zhang, X.; Lv, Z.; Weng, J.; Fan, M.; Fan, F.; Wang, X.; Chen, X.; Shi, S.; Shen, X. Enhanced Mechanical and Thermal Properties of Waste Electric Porcelain-Based Solar Energy-Absorbing Thermal Storage Ceramics with Interwoven Mullite Structure. *Crystals* **2025**, *15*, 90. https://doi.org/10.3390/cryst15010090

1. Introduction

With the development of the electric power industry, electric porcelain has become the most widely used insulator material. The increase in electric porcelain production has led to an increase in waste [1–4]. The accumulation of global waste electric porcelain has reached tens of millions of tons, resulting in the waste of resources, land occupation and environmental protection problems. Therefore, more and more researchers are engaged in the recycling of waste electric porcelain [5–8]. Wang et al. [9] successfully prepared high-temperature heat-resistant materials based on waste electric porcelain using a pressureless sintering method, and found that the samples sintered at 1250 °C and with a 30 wt.% kaolin addition had the best overall performance, demonstrating a flexural strength of 32.83 MPa and a compressive strength of 89.59 MPa, which provided experimental bases for tests of high-value utilization and the recycling of waste electric porcelain. Pivák et al. [10]

investigated low-carbon composites based on MOC, silica sand, and ground insulator waste and found that the addition of waste electric porcelain improves the mechanical strength and reduces the thermal conductivity of the materials, providing a new avenue for the development of environmentally friendly building materials. López-Perales et al. [11] recycled industrial waste porcelain (chamotte waste) in the manufacture of porcelain stoneware, partially replacing quartz and feldspar in a triaxial system, and found that the addition of 15% waste porcelain to the new ceramic formulations significantly improved the material properties, obtaining the best technical characteristics, including a density of 2.41 g/cm^3, a linear shrinkage rate of 11.2%, a water absorption of 0.08%, a mechanical strength 314.94 MPa, and a microhardness 7.07 GPa. Talaei et al. [12] conducted a study on the mechanical properties of fiber-reinforced concrete incorporating waste porcelain aggregates under elevated temperatures. They discovered that the incorporation of steel fibers notably enhanced the concrete's thermal resistance and compressive strength. Meanwhile, polypropylene fibers were found to be effective in preventing concrete spalling. These findings underscore the significant potential for enhancing the utilization of waste electrical ceramics, but there are significant shortcomings in terms of high value.

The main components of waste ceramics are aluminum oxide (Al_2O_3) and silicon oxide (SiO_2), which are highly consistent with the material composition required for solar absorption and thermal storage integrated ceramics (SATS ceramics) [13–19]. With the development of concentrated solar power (CSP) technology, there is an increasing demand for highly efficient heat-absorbing and energy-storing materials with excellent heat-absorbing properties, good thermal stability, and thermal shock resistance to cope with the high temperatures and thermal cycling conditions of CSP systems [20–23]. Lao et al. [21] significantly improved the thermal storage capacity of the material by encapsulating an Al-Si alloy (latent heat material) in a SiCw/Al_2O_3 honeycomb ceramic (heat-sensing material). This enhanced the storage capacity by more than 114%, which demonstrates the advantages of ceramic materials for high-temperature sensible heat storage. Xu et al. [24] investigated the preparation of solar thermal storage ceramics using high-calcium high iron steel slag and 10% cordierite, which had the best performance when sintered at 1240 °C, with a flexural strength of 92.52 MPa, which was enhanced to 97.06 MPa after 30 thermal shock cycles (an increase of 4.91% over the pre-temperate shock) and a thermal storage density of 867.95 kJ/kg. In contrast, the present study utilizes solid waste and reduces the cost of production, as shown by the price comparisons in Table 1.

Table 1. Price comparisons with Xu et al. [24].

Raw Materials Used in This Experiment	Price/ ¥/Tonne	Raw Materials Used by Xu et al. [24]	Price/ ¥/Tonne
Waste Electric Porcelain (45 wt.%)	100	Bauxite (50 wt.%)	1800
Bauxite (45 wt.%)	1800	Kaolin (50 wt.%)	2500
Kaolin (10 wt.%)	2500	Iron Oxide (11 wt.%)	7000
Magnetite (9 wt.%)	880		
Total Price	1184.2	Total Price	2920

According to Hasselman's theory, the flexural strength (σ) is proportional to the thermal stress fracture resistance parameter R. Therefore, the thermal properties of the material can be indirectly reflected through and the relationship can be expressed by the equation:

$$R = \Delta T = \sigma (1 - v)/E\alpha$$

where ΔT is the critical temperature. It can be seen that the higher the flexural strength, the better the thermal performance of the material [25] and the more suitable it is for high temperature working environments. Improving the microstructural refinement and densification of the Al_2O_3 matrix can enhance the flexural strength of ceramics prepared

by pressureless sintering. This improvement can be achieved by introducing sintering additives, such as alkaline-earth metal oxides (MgO), transition-metal oxides (TiO_2, Fe_2O_3), and rare-earth oxides (Y_2O_3, Sm_2O_3, La_2O_3, etc.) [26].

At present, the research on the comprehensive utilization of waste electric porcelain mainly focuses on building materials, but its application in the field of solar thermal storage materials has yet to be studied in depth [12,27–30]. Waste electric porcelain is mainly divided into blanks and glazes [17]. The blanks' composition is similar to that of heat storage ceramics, and the glaze composition is similar to the sintering additives used in heat-storage ceramics, so waste electric porcelain has great feasibility in the preparation of high-strength STAS ceramic materials [31]. Mature ceramic materials are subjected to thermal stresses in high-temperature environments, which can lead to thermal cracking and a reduction in energy storage capacity. This phenomenon results in a limited range of applications for ceramic materials at elevated temperatures. In this study, specific heat capacity tests reveal that the samples demonstrate commendable performance under high-temperature conditions, thereby offering favorable prospects for use in high-temperature working environments. The aim of this study is to explore the potential application of waste electric porcelain in heat absorption and energy storage materials, and to develop a low-cost, high mechanical strength SATS material by comprehensively examining the chemical composition, physical properties, and thermophysical properties of waste electric porcelain. The study will comprehensively examine the effects of additives and sintering temperature on mechanical properties, linear shrinkage rate, bulk density, water absorption, porosity, and ignition loss rate. The final flexural strength of the material was determined to be 96.05 MPa, while Wang et al. reported a strength of 32.83 MPa and Xu et al. reported 92.52 MPa. Clearly, our materials satisfy the performance standards set by the industry. This study provides a method for the production of low-cost and high-performance SATS materials from waste electric porcelain.

2. Materials and Methods

2.1. Raw Materials

In this study, waste electric porcelain (produced in Shandong, China), bauxite (produced in Zhengzhou, Henan, China), and kaolin were used as raw materials. Magnetite (Lingshou County Qiangdong Mineral Processing Factory, Shijiazhuang, China) was used as an additive and polyvinyl alcohol (PVA, Aladdin, Shanghai, China) as a binder. The formulations are shown in Table 2.

Table 2. Formulations of samples (wt.%).

Ingredient	Waste Electric Porcelain	Bauxite	Kaolin (Clay)	Magnetite (Fe_3O_4, Addition)	PVA (Addition)
BK0	45	45	10	0	5
BK1				5	
BK2				7	
BK3				9	
BK4				11	
BK5				13	

2.2. Preparation Process

According to the designed BK series formulation, the various components were accurately weighed and the samples were prepared according to the sample preparation process shown in Figure 1. The STAS ceramic samples were prepared after mixing, granulation (bound by PVA), followed by dry-pressing molding, drying (in a DGT-G80 blower drying oven), and sintering (in a KSL1700 type resistance furnace). Mixing is done to avoid product defects due to uneven distribution of components and to make each part of the sample consistent in its properties and

behavior. Pelletizing is done to enhance the bonding between particles so that the particles are better held together when subjected to pressure, thus improving the hardness and stability of the sample. Dry compression molding is done to form a dense molded body of the sample to facilitate testing of its properties. Drying is done to remove moisture from the sample and thus avoid errors in measuring the rate of loss on burnout. The purpose of sintering is to densify the raw billet via high temperature treatment to improve its mechanical strength and physical properties, while stabilizing the chemical properties in order to obtain a ceramic material with excellent properties. The size specifications of the prepared samples are as follows: the slab sample size is 45.50 mm (length) × 6.50 mm (width).

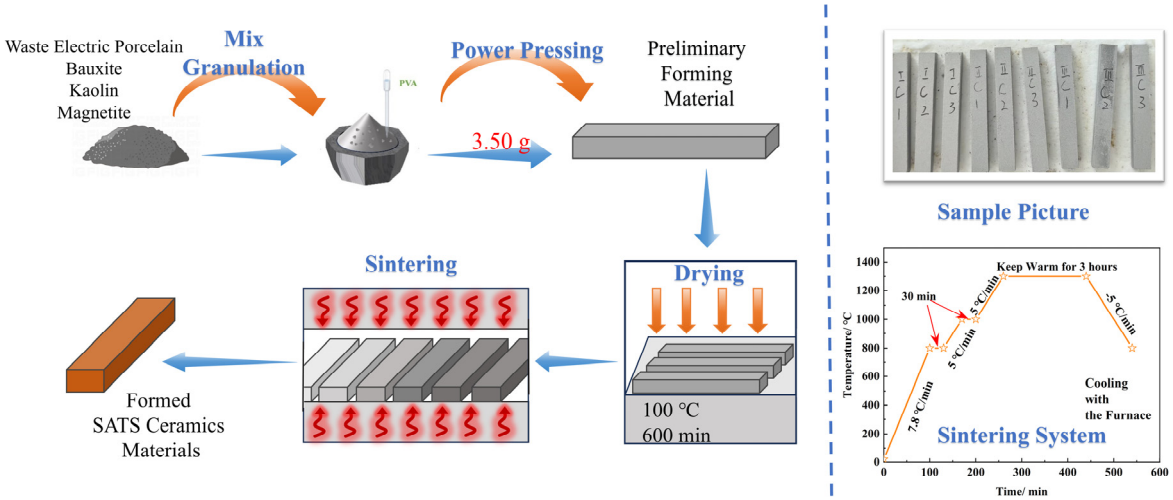

Figure 1. Sample preparation process.

Based on the phase diagram of the silica-alumina-solute system [32], it is understood that a large number of liquid phases are formed in the sample at temperatures greater than 1600 °C. When the rate of liquid phase production is greater than the rate of new phase production, over-sintering occurs, resulting in melting of the material [33]. Therefore, the sintering temperatures were set to 1100 °C, 1200 °C, 1300 °C, 1400 °C, and 1500 °C. It was found that when the sintering temperature was 1500 °C, the samples melted, and the more magnetite the sample contained the more serious the melting was.

2.3. Characterization

Material phase analysis was carried out using an X-ray diffractometer (XRD, Rigaku Smartlab, Akishima-shi, Japan) with a step scanning speed of 5°/min and a measurement angle range of 5–80° to determine the phase composition. The microstructure of the samples was observed using a scanning electron microscope (SEM, ZEISS Sigma 360, Jena, Germany). An X-ray fluorescence spectrometer (XRF, EDX4500H, Jiangsu, China) was used to determine the material composition and elemental ratios. The specific heat capacity of the samples was analyzed using a differential scanning calorimeter (HS-DSC-100, Shanghai, China) with a ramp rate of 10 °C/min.

The bulk density, porosity, and water absorption of the samples were determined by the boiling method and Archimedes drainage method, according to the GB/T 3810.3-2016 standard. The flexural strength of all the sintered samples was tested by the three-point flexural method using a universal material testing machine (WDW-3T, Jinan, China) according to the GB/T 38978-2020 standard. The falling speed of the force arm for the flexural strength test was uniformly set at 0.05 mm/min. The same batch of raw materials was used for all testing, and all testing was performed using the same pressure tablet (10 MPa, 1 min), and the same experimental apparatus to minimize experimental errors. Meantime, the physical property tests

of the samples were conducted three times. The final data were derived by calculating the mean and standard deviation of these test results, thereby enhancing the accuracy and reliability of the findings. By considering the mass and length of the tested samples, the linear shrinkage rate and ignition loss rate can be accurately calculated.

The linear shrinkage rate can be calculated from the change in length using the following formula:

$$L_\sigma = \frac{L_0 - L_n}{L_0} \times 100\%$$

where L_σ is the linear shrinkage rate, %; n = 0, 1, 2, 3, 4, 5; L_0 is the initial length, g; and L_n is the sintered length, g.

The ignition loss rate allows for the calculation of the amount of loss on burn, which is calculated using the following formula:

$$m_\sigma = \frac{m_0 - m_n}{m_0} \times 100\%$$

where m_σ is the ignition loss, %; n = 0, 1, 2, 3, 4, 5; m_0 is the initial mass, g; and m_n is the mass after sintering, g.

3. Results and Discussion

3.1. Compositional and Mineralogical Analysis of Raw Materials

Table 3 presents the chemical composition analysis of the raw materials utilized in the study. The results indicate that the waste electric porcelain material contains 50.20% silicon oxide (SiO_2) and 29.15% aluminum oxide (Al_2O_3) by weight. In contrast, the bauxite material comprises 79.19% SiO_2 and 2.78% Al_2O_3. Additionally, both materials are characterized by the presence of 5.37% ferrous oxide (FeO), 7.47% potassium oxide (K_2O), and 9.42% titanium oxide (TiO_2). These constituents play a significant role in the sintering process and the subsequent properties of the ceramics produced.

Table 3. Chemical composition of raw materials (wt.%).

Raw Materials	Al_2O_3	SiO_2	FeO	K_2O	CaO	TiO_2	MgO	MoO_3	i.t.
Waste Electric Porcelain	50.203	29.155	5.373	6.045	1.775	2.578	1.11	1.468	2.289
Bauxite	79.192	2.782	-	1.431	2.112	6.854	1.25	1.088	5.289
Kaolin	49.147	35.086	6.527	0.738	0.868	2.548	0.91	1.589	2.591
Magnetite	2.099	4.323	85.28	1.28	2.199	0.993	0.15	0.62	3.057

Alkaline metal oxides, such as potassium oxide (K_2O), present in the raw materials, are known to lower the sintering temperature. They facilitate the formation of a liquid phase, which fills the material's voids and encourages the growth of mullite crystals, thereby enhancing the material's structural strength [34]. Furthermore, the inclusion of transition metal oxides, such as ferrous oxide (FeO), in the raw materials also contributes to the enhancement of the material's mechanical strength [35,36]. Titanium oxide (TiO_2) plays a role in promoting the rapid in situ growth of mullite crystal columns within the material, which in turn further bolsters the material's mechanical strength [37]. Concurrently, magnetite (Fe_3O_4) reacts with silicon oxide (SiO_2) at high temperatures to produce solid solutions with low melting points. These solid solutions induce deformation in the lattice structure of the material, effectively preventing deformation caused by external forces and thus significantly improving the material's mechanical strength.

As depicted in Figure 2, the primary phase compositions of waste electric porcelain are mullite, corundum, and α-quartz. In contrast, bauxite and kaolin are predominantly composed of corundum, α-quartz, and kaolin phases. The presence of corundum (Al_2O_3)

and mullite ($3Al_2O_3 \cdot 2SiO_2$) is crucial for enhancing sintering characteristics, minimizing volumetric shrinkage, and ensuring the material's stability at high temperatures [38]. These phases are instrumental in bolstering the mechanical properties and thermal stability of the sintered body, which are critical attributes for materials intended for high-temperature structural applications.

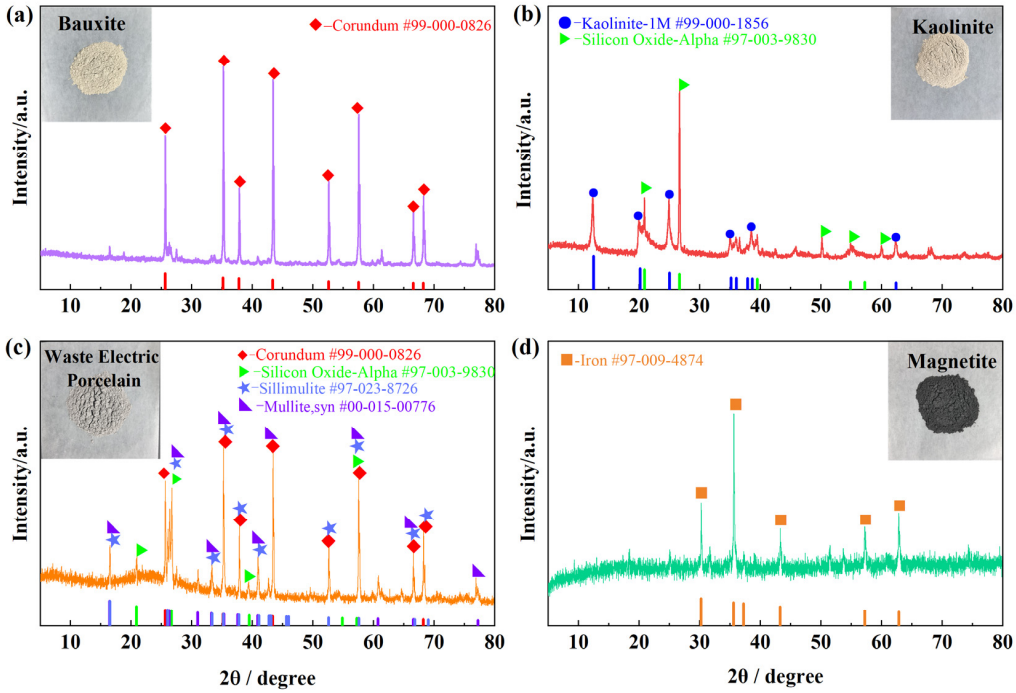

Figure 2. XRD analysis of raw materials: (**a**) bauxite; (**b**) kaolinite; (**c**) waste electric porcelain; (**d**) magnetite.

The material's high content of silicon (Si) and aluminum (Al) is essential for the formation of the mullite phase, which significantly enhances the specimen's performance under high-temperature conditions. Mullite is well-known for its excellent mechanical properties and thermal stability, rendering it a vital component in improving the high-temperature capabilities of ceramic materials. The inclusion of magnetite (Fe_3O_4), which is primarily a metallic phase, significantly contributes to reducing the sintering temperature of the samples and increasing their density. At high temperatures, Fe_3O_4 reacts with SiO_2 to form a low melting point solid solution, which facilitates the sintering process by lowering the required temperature. Additionally, the magnetic properties of Fe_3O_4 enhance the density and mechanical properties of the materials. The phase compositions of the samples are consistent with the chemical composition analysis presented in Table 3, thereby confirming the suitability and potential of raw materials like waste electric porcelain and bauxite for the fabrication of high-temperature structural materials.

3.2. Effect of Sintering Temperature on Sample Properties

In order to investigate the effect of sintering temperature on the phase composition of the samples, we performed XRD tests on the sintered samples [39]. Figure 3 demonstrates the results of the phase composition of the samples at different sintering temperatures. From Figure 3, it can be clearly observed that the main crystalline phases of the samples after sintering at different temperatures are mullite and corundum phases, accompanied by a small amount of quartz phase, which is consistent with the phase composition before sintering. The intensities of the diffraction peaks for the primary mullite phase escalated with the rise in sintering temperature, signifying that an elevated sintering temperature is conducive to enhancing the crystallinity of mullite. Concurrently, the augmentation of

the mullite phase coincided with a diminishing presence of Al_2O_3 and SiO_2, resulting in a progressive reduction of the corundum and quartz phases.

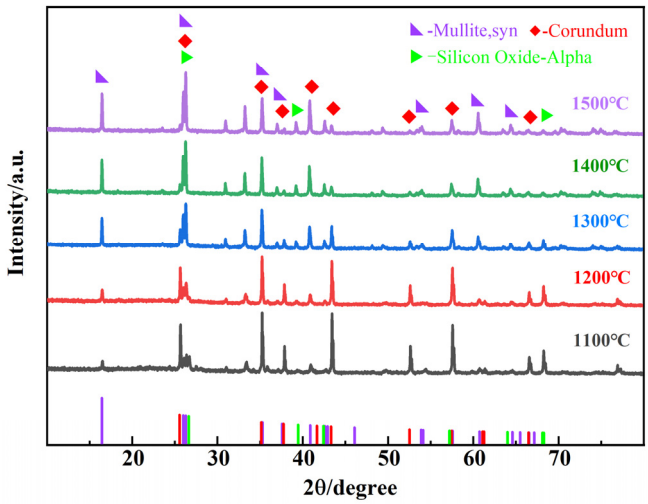

Figure 3. XRD patterns of samples at different sintering temperatures.

The findings underscore the pivotal role of sintering temperature in influencing the phase composition of the samples. The promotion of mullite phase crystallization through high-temperature sintering is likely attributed to the thermal stability of mullite and its growth kinetics at elevated temperatures. Concurrently, the consumption of Al_2O_3 and SiO_2 at high temperatures impacts the stability of other phases, resulting in a decrease in the corundum and quartz phases. These transformations in phase composition directly influence the microstructure and the resulting macroscopic properties of the samples, highlighting the importance of sintering temperature in the development of ceramic materials with desired performance characteristics.

Figure 4 delineates the patterns of the linear shrinkage rate and ignition loss rate for the samples across various sintering temperatures [40]. Initially, the linear shrinkage rate escalates with temperature, a result of enhanced inter-particle bonding and diminished porosity throughout the sintering process. Notably, between 1100 °C and 1200 °C, the significant formation of the mullite phase results in a pronounced increase in the linear shrinkage rate. However, beyond 1200 °C, this rate begins to decline, potentially due to the proliferation of the liquid phase within the samples, which alters the sintering dynamics. Sintered at 1500 °C, the linear shrinkage rate becomes negative, indicative of sample deformation resulting from over-burning. Concurrently, ignition loss rate generally increases with temperature but remains within a narrow range of 1.5% to 2.5%, with a maximum variance of 2.32%. This increase in ignition loss rate is attributed to the thermal decomposition of kaolin and the progressive release of volatiles, particularly sintered at 1500 °C, where over-burning leads to the emergence of multiple liquid phases. These trends directly reflect the physical and chemical transformations occurring within the samples during sintering, which are intricately linked to the microstructure and phase composition. Such transformations are critical for optimizing the samples' physical properties and enhancing their mechanical and thermal stability.

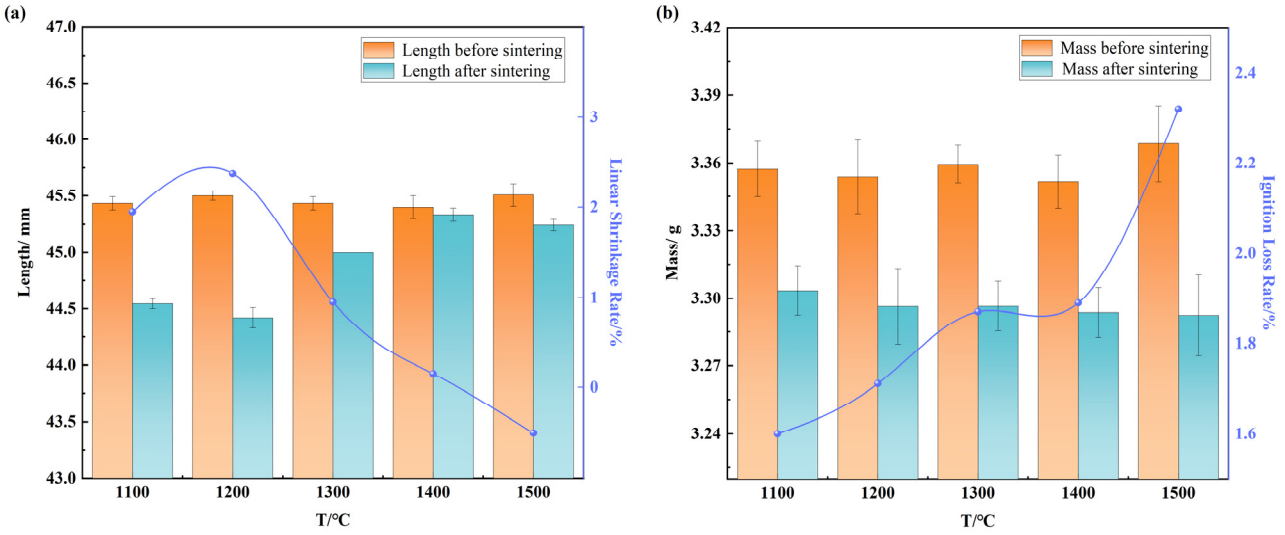

Figure 4. (**a**) Linear shrinkage rate and (**b**) ignition loss rate of samples at different temperatures.

Figure 5a illustrates the changes in the bulk density, porosity, and water absorption of the samples with varying sintering temperatures. Porosity has a significant effect on the mechanical properties, thermal conductivity, and thermal shock properties of the material. An appropriate pore size can optimize the impact resistance of the material, but too large of a pore size will reduce its mechanical strength and thermal conductivity. In this paper, we explore the optimal conditions for preparing the samples by testing the porosity of the samples.

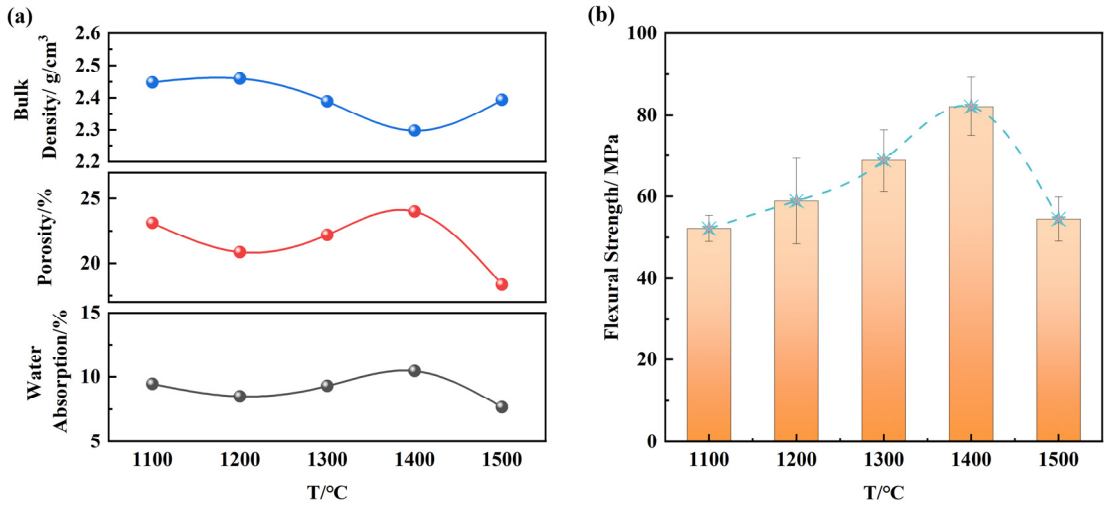

Figure 5. (**a**) Bulk density, porosity and water absorption, (**b**) flexural strength of sintered samples at different temperatures.

The porosity initially decreases with increasing temperature, then increases, and finally decreases again. Notably, above 1200 °C, porosity rises from 20.9% to 24.0%. However, beyond 1500 °C, porosity diminishes, which is attributed to over-burning above this temperature, leading to the generation of a substantial liquid phase that fills the pores. Pore formation during the molding process is identified as the primary defect, with closure defects being of secondary concern. In conjunction with XRD analysis, it is postulated that pore formation correlates with the development of mullite structures. This process necessitates the consumption of Al_2O_3 and SiO_2 from the raw materials to form mullite columns, consequently creating pores. Furthermore, the reduction in bulk density is ascribed to the proliferation of internal porosity, yet the overall fluctuation stays within the 2.3–2.5 g/cm^3 range, exerting a minimal impact on flexural strength. Figure 5 illustrates that as the temper-

ature increases, porosity initially decreases before subsequently increasing. This behavior may be attributed to the addition of PVA, which, due to its high viscosity, may not have been adequately controlled in terms of its ratio. As the PVA burns out, porosity increases. In contrast to Figure 5b, the flexural strength increases rather than decreases, likely due to the significant increase in the mullite phase with rising temperature, which enhances the stability of the sample's lattice structure. Furthermore, the uniform distribution of pores may contribute to a more even stress distribution when the sample is subjected to external forces, reducing the likelihood of stress concentration and consequently enhancing the sample's strength. Water absorption is directly proportional to porosity and inversely proportional to bulk density, reflecting the interplay between these properties and their influence on the material's performance.

Figure 5b presents the flexural strength of the samples across a range of sintering temperatures. The data reveal that the mechanical properties of the samples improved with the elevation of temperature, culminating in an optimal flexural strength of 82.12 MPa sintered at 1400 °C. This enhancement in mechanical performance is particularly pronounced at this temperature. The bulk density of the samples in this experiment varies less, and the main reason for the effects on the flexural strength is the interlocking of the mullite phases. As illustrated in Figure 6, the XRD results were analyzed semi-quantitatively for the mullite and corundum phases at different temperatures. It was observed that the increase in the content of the mullite phase correlated with an enhancement in the flexural strength of the samples. The presence of the mullite phase is a critical factor influencing the high-temperature strength of the material. Based on the comprehensive analysis of the physical properties of the BK series samples, it is concluded that the optimum sintering temperature for the BK series samples is 1400 °C.

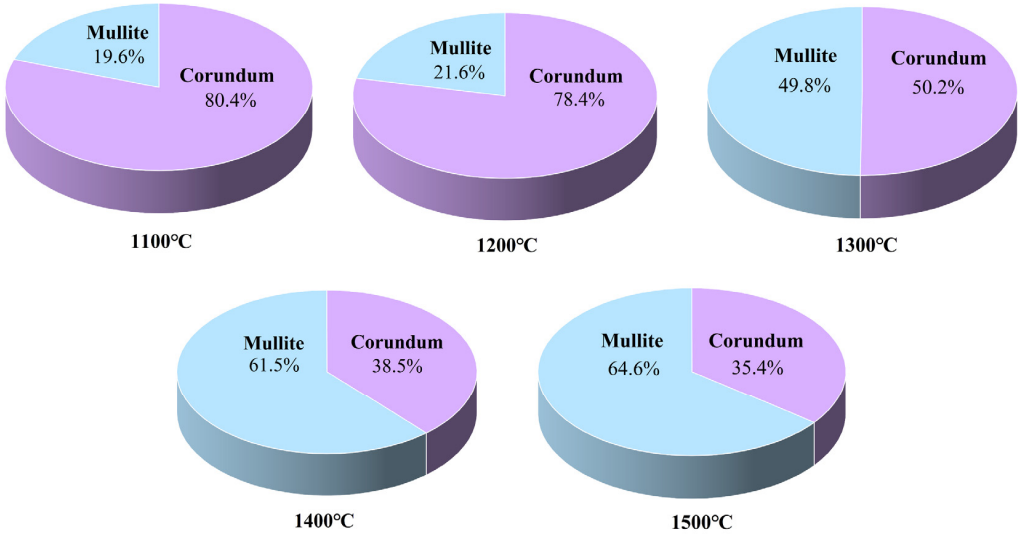

Figure 6. Comparison of semi-quantitative analyses of mullite and corundum phases at different temperatures.

To delve into the impact of sintering temperature on the microstructure of STAS ceramics samples, we conducted SEM tests on the cross-sections of the samples. Figure 7 displays the outcomes of these tests, highlighting the influence of sintering temperature on the sample microstructure. Sintered at 1100 °C, the samples initiate the formation of a mullite structure, where mullite columns fill the pores, resulting in a progressive reduction of porosity and a concurrent increase in flexural strength, aligning with the findings presented in Figure 5. As the sintering temperature continues to rise, the mullite columns expand, and their length-to-diameter ratio increases, signifying that elevated sintering temperatures foster the growth of mullite crystals. This observation underscores

the role of temperature in enhancing the crystallization and structural development of mullite, which is pivotal for the microstructural evolution and mechanical performance of STAS ceramics.

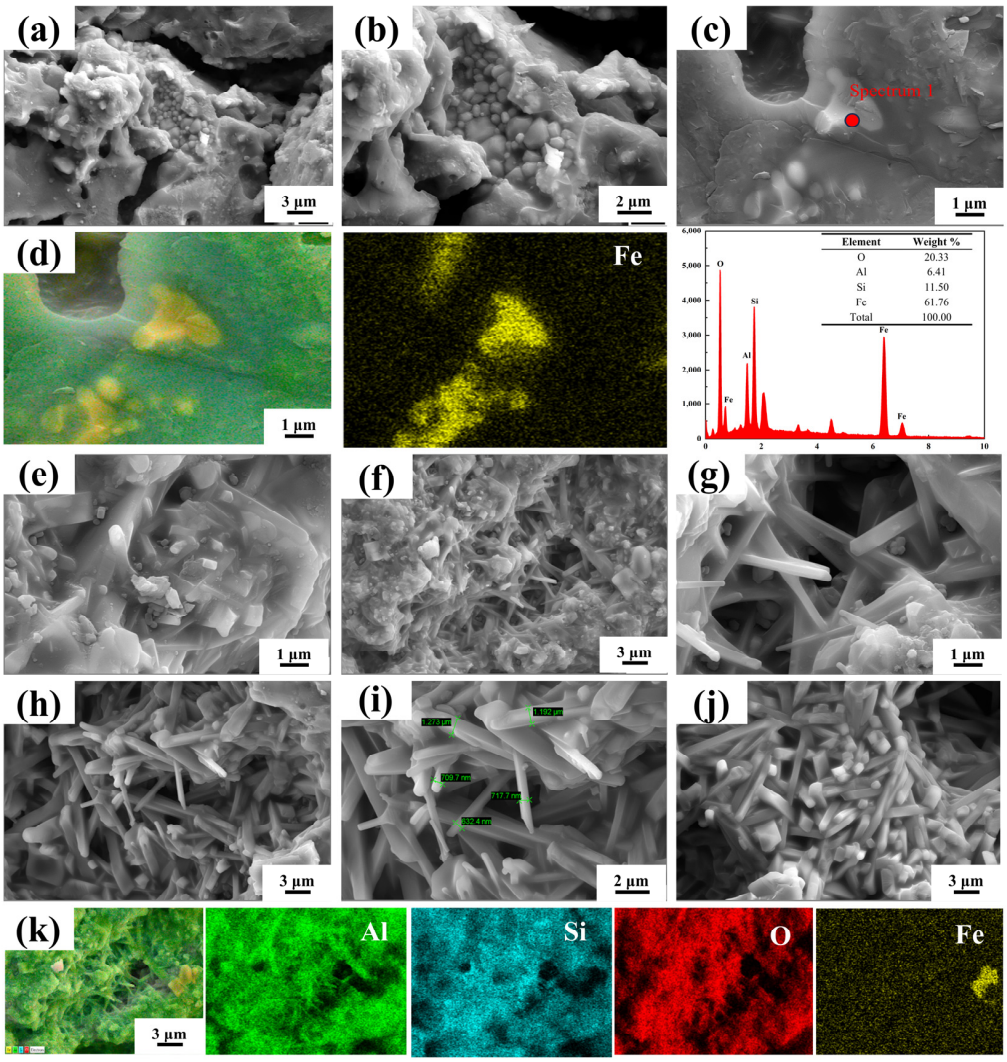

Figure 7. SEM and EDS images of samples fired at different sintering temperatures: (**a**,**b**) 1100 °C; (**c**,**d**) 1200 °C; (**e**–**g**,**k**) 1300 °C; (**h**,**i**) 1400 °C; (**j**) 1500 °C.

The subdued mechanical properties of the samples at lower temperatures can be partially attributed to the enrichment of iron (Fe) elements. The accumulation of Fe elements enhances the brittleness of the ceramic samples, consequently diminishing their mechanical properties [41]. A comparative analysis between Figure 7d,k reveals that as the temperature increases, the distribution of Fe elements becomes more uniform, which significantly mitigates the brittleness and enhances the mechanical properties of the samples. Observations from Figure 7g–j demonstrate that the mullite structure undergoes progressive densification, with the mullite column structure reaching maturity sintered at 1400 °C, characterized by diameters ranging from approximately 632.4 nm to 1.273 μm. The interlaced mullite structure, indicative of robust mechanical properties, corroborates the flexural strength data, providing substantial evidence for the material's performance capabilities.

Sintered at 1500 °C, however, the mullite began to aggregate, accompanied by the emergence of irregular deep holes. This phenomenon is attributed to the substantial liquid phase generated within the specimen, which, upon cooling, induces significant shrinkage, leading to the formation of pores and consequently reducing the mechanical strength. This observation aligns with the results pertaining to bulk density, porosity, and water

absorption, as well as the flexural strength outcomes. Collectively, these findings underscore that the sintering temperature exerts a profound influence not only on the crystallographic growth and microstructural densification of mullite but also on the mechanical properties and pore characteristics of STAS ceramics. This highlights the critical role of sintering temperature in determining the overall performance and quality of the STAS ceramics.

3.3. Effect of Magnetite Content on Sample Properties

Figure 8 shows the results of the phase composition of the samples of the BK series sintered at 1400 °C. From Figure 8, it can be seen that the main phase present in the prepared SATS ceramics material is mullite, and a very small amount of corundum phase. The increase in magnetite content accelerates the growth rate of the mullite structure, consuming a large amount of Al_2O_3 and SiO_2, to the extent that the phase composition contains very little corundum phase and almost no quartz phase.

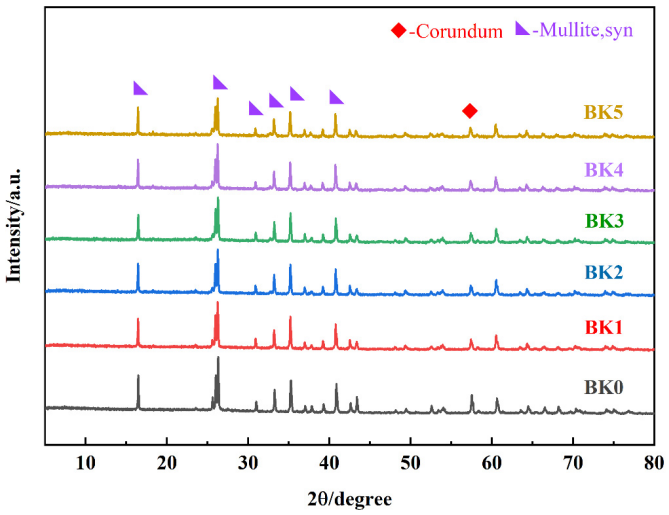

Figure 8. XRD images of samples sintered at 1400 °C for BK series samples.

Figure 9 illustrates the changes in linear shrinkage rate and ignition loss rate with respect to magnetite content for the BK series samples sintered at 1400 °C. As is made evident in Figure 9a, the linear shrinkage rate of the samples escalates with an increase in magnetite content. This trend can be ascribed to the Fe element's role in augmenting the glassy phase within the samples, which in turn diminishes the viscosity of the liquid phase and accelerates the mass transfer rate. The enhanced mass transfer, coupled with the increased glassy phase, fosters the development of mullite structures. Consequently, the heightened consumption of Al_2O_3 and SiO_2 due to mullite formation results in a higher linear shrinkage rate for the samples. This relationship underscores the impact of magnetite content on the sintering behavior and microstructural evolution of the BK series samples.

Furthermore, Figure 9b delineates an overall downward trend in the ignition loss rate of the samples as the magnetite content increases, with the maximum difference recorded at 1.99%. This reduction in ignition loss rate is likely due to the fact that the addition of magnetite enhances the densification of the samples, thereby diminishing the content of volatiles and consequently decreasing the sintering loss. This pattern suggests that an increase in magnetite content significantly influences the sintering behavior and the resulting microstructure of the samples. Lower ignition loss rate not only reduces heating energy consumption but also reduces sintering cycles and improves energy efficiency. Such an influence is crucial for refining the sintering process to achieve improved material properties. The optimization of magnetite content can lead to enhanced densification and

reduced porosity, which are key to attaining superior mechanical strength and thermal stability in the final ceramic products.

Figure 10a illustrates the changes in bulk density, porosity, and water absorption of the BK series samples at a sintering temperature of 1400 °C in relation to the content of magnetite. With an increasing content of magnetite, there is a gradual reduction in the porosity of the samples, accompanied by a corresponding increase in bulk density, although the overall variation is not markedly substantial. This pattern indicates that the incorporation of magnetite is instrumental in decreasing the porosity within the samples, which in turn leads to an increase in their bulk density. The relationship between water absorption and porosity is directly proportional, while it is inversely proportional to bulk density, highlighting the interplay between these properties and their impact on the material's behavior and performance.

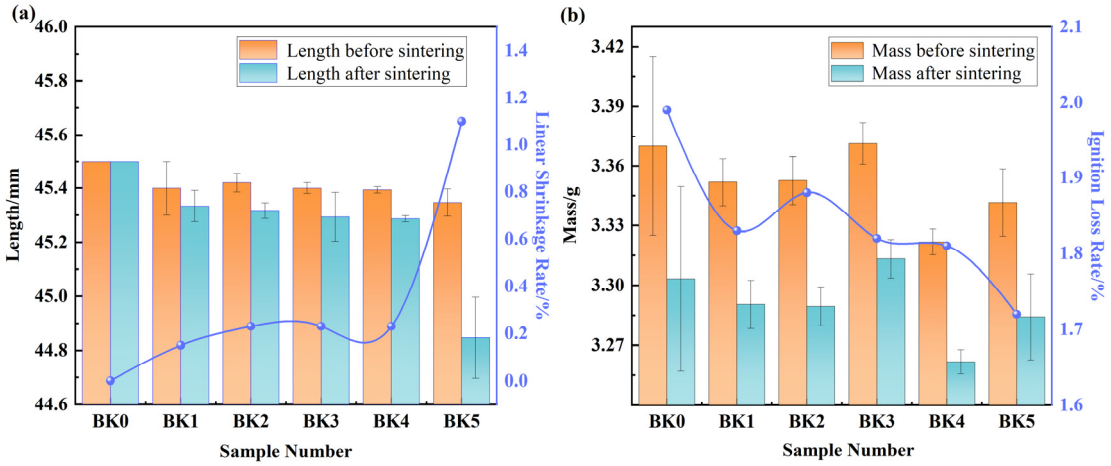

Figure 9. (**a**) Linear shrinkage rate and (**b**) ignition loss rate of sintered specimens at 1400 °C for BK series samples.

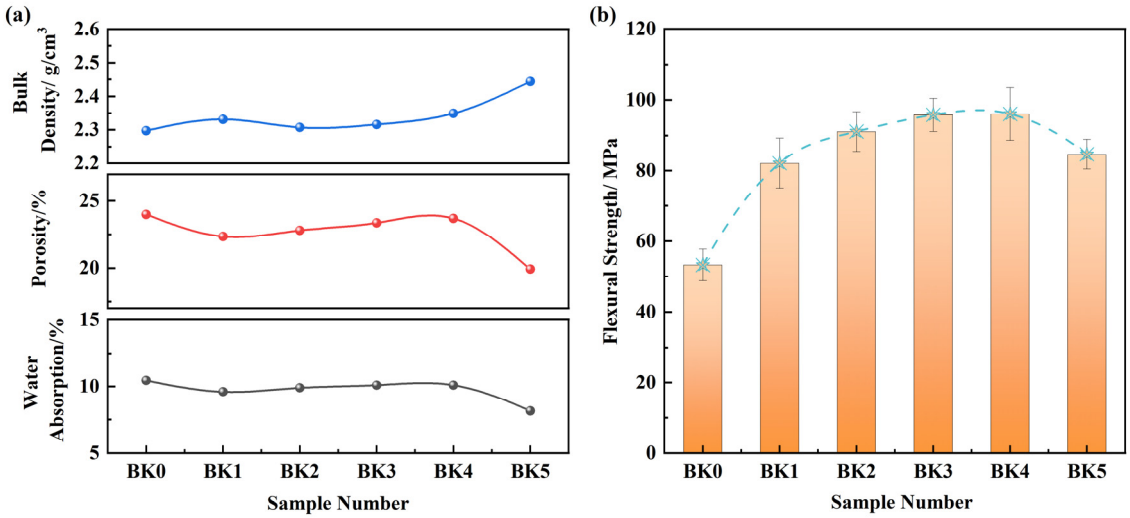

Figure 10. (**a**) Bulk density, porosity and water absorption, (**b**) flexural strength of sintered samples at 1400 °C temperature for BK series samples.

Figure 10b elucidates the trend of increasing flexural strength in the samples with the increment of magnetite content, ascribed to the Fe element's contribution to enhanced densification. Notably, the specimen BK4 achieved the highest flexural strength of 96.05 MPa, demonstrating the optimal performance among the series. Conversely, the specimen BK5 exhibited a decline in flexural strength, which can be attributed to the reduced suitability of the sintering temperature with the increased content of Fe_3O_4. BK5 samples are susceptible

to over-burn at sintering temperatures of 1500 °C or more. Over-burning is characterized by a reduction in the viscosity of the liquid phase and the decomposition of mullite at high temperatures, resulting in matrix deformation, elevated bulk density, and a consequent decrease in flexural strength. The findings presented in Figure 10 underscore the effectiveness of Fe_3O_4 addition within an appropriate content range in enhancing the physical properties of the samples. This includes the reduction of porosity, the increase in bulk density, and the improvement of flexural strength, thereby highlighting the significance of magnetite content in tailoring the microstructure and mechanical properties of the BK series samples.

Figure 11 displays the SEM images of the BK series samples sintered at 1400 °C. Figure 10a, captured at high voltage and low magnification, reveals that the porosity of the samples remains largely unchanged, corroborating the findings from Figure 10. Nonetheless, it is observed that as the magnetite content decreases, the porosity becomes finer and more densely packed. This phenomenon is attributed to the increased presence of Fe elements, which boost the mass transfer rate, expedite the growth of mullite columns, and deplete Al_2O_3 and SiO_2, thereby forming pores. Additionally, the elevated Fe content may also induce sample shrinkage, contributing to pore formation. These SEM observations provide a clear understanding of how microstructural changes with magnetite content affect the material's properties.

Figure 11b illustrates that the mullite structure transitions from a disordered to an ordered arrangement with increasing magnetite content, achieving an optimal state at an 11 wt.% magnetite content. The mullite structure in the BK0 samples exhibits a haphazard growth pattern, presenting as thick, irregularly shaped rods of varying lengths. Conversely, the addition of a small amount of magnetite to samples BK1 and BK2 leads to a pronounced and rapid elongation of the mullite columns. Specifically, the diameter of the mullite columns in sample BK1 spans from 632 nm to 1.273 μm, and in sample BK2 it extends from 883 nm to 1.540 μm. These findings indicate that an elevated magnetite content can significantly expedite the formation of mullite columns, highlighting the influence of magnetite on the microstructural development and the enhancement of material properties.

Continuing the examination of the BK3 and BK4 samples, it is evident that with the increase in magnetite content, the mullite structure forms into short, clustered formations with an interlaced pattern, which aligns with the observed flexural strength of the samples. The interlaced mullite grains form a compact mesh structure that effectively disperses stress and reduces stress concentration, significantly enhancing the material's strength. Additionally, this configuration establishes a continuous heat conduction pathway, minimizing scattering and reflection during thermal transfer, which subsequently improves the material's thermal conductivity. In addition, the interlocking grains constrain each other and reduce the deformation during thermal expansion, thus improving the thermal stability of the material. Under rapid temperature fluctuations, this interlaced structure can absorb and distribute thermal stresses, reducing stress concentration, effectively preventing crack formation and significantly improving the material's thermal shock resistance. This is compatible with the working environment of the material. However, a further increase in magnetite content, and consequently in Fe element concentration, results in increased brittleness of the samples. At the 13 wt.% magnetite content level, the EDS image shown in Figure 11c indicates an enrichment of Fe elements on the mullite columns, which correlates with a decrease in the sample's mechanical strength.

Taking into account the flexural strength data, the sample with 11 wt.% magnetite content was identified as having the optimal performance. EDS image analysis revealed a uniform distribution of elements within the sample, particularly the Fe element, which lacked any significant enrichment, effectively mitigating the sample's brittleness. In conjunction with XRD image analysis, it was confirmed that the predominant phase in the

sintered samples was the mullite phase, aligning with the SEM image findings. This consistency further validates the influence of magnetite content on the microstructural development and the resultant properties of the samples.

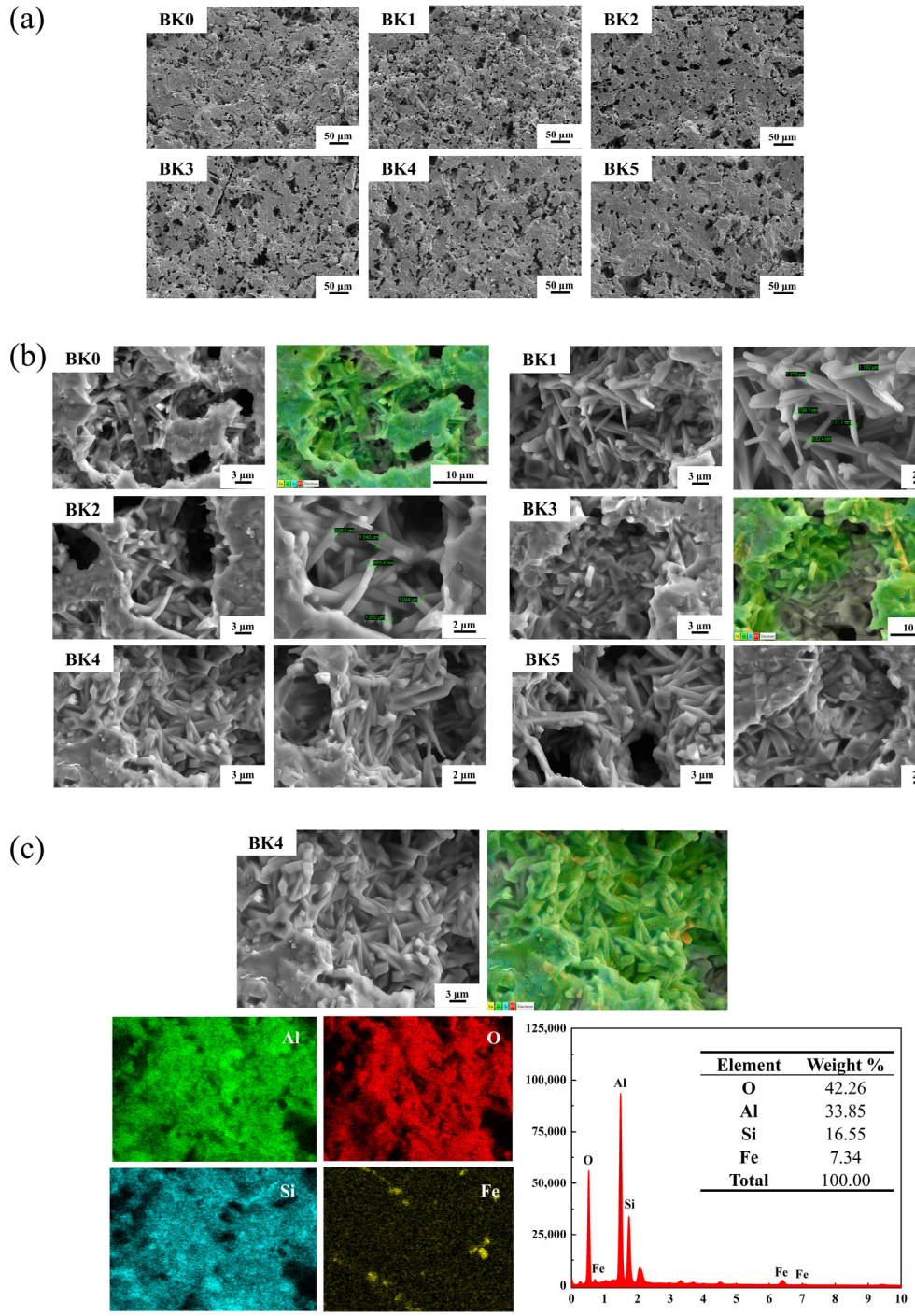

Figure 11. SEM and EDS images of samples sintered with different ratios: (**a**) SEM images with of 200×; (**b**) SEM images with of 3000× and 6000×; (**c**) SEM and EDS image of the BK4 sample.

The thermophysical properties of STAS ceramics are pivotal for their efficacy in high-temperature settings [42–44]. An in-depth thermophysical analysis has been conducted on the BK series samples, specifically BK1 through BK5, which were sintered at their optimal sintering temperatures. Figure 12 presents the specific heat capacity (Cp) measurements of these BK series samples, spanning from room temperature to 300 °C. The observed gradual increase in Cp values with rising temperature underscores the enhanced thermal storage

capability of these ceramics. An elevated Cp value signifies an improved thermal storage capacity, which is advantageous for high-temperature applications [45,46]. Specific heat capacity is influenced not only by porosity and bulk density but also by the presence of discontinuous solid and glass phases [47]. Initially, an increase in the Fe element content, which corresponds to a rise in magnetite, leads to a decrease in the specific heat capacity of the samples. However, as the mullite phase increases, the specific heat capacity begins to rise. Beyond 280 °C, sample BK4 exhibits the highest specific heat capacity.

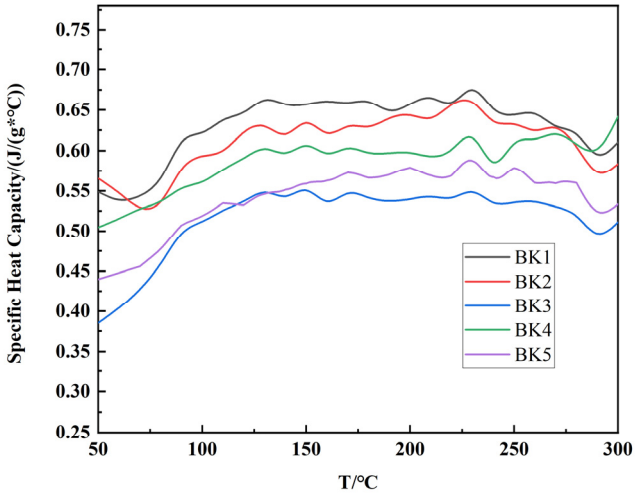

Figure 12. Specific heat capacity of BK series samples sintered at optimum temperature of 1400 °C.

Among the samples, BK1 demonstrates the highest Cp in the lower temperature range, from room temperature to 280 °C, while BK4 excels in the higher temperature range, between 280 °C and 300 °C, with a specific heat capacity of 0.6415 J/(g* °C) at 300 °C. Notably, sample BK4 shows better Cp values in the high temperature range, making it the sample with the best thermophysical properties. In summary, a higher specific heat capacity translates to a better-suited thermal storage system, which could potentially reduce the size of the system and enhance its thermal storage efficiency.

4. Conclusions

In this study, the preparation process and properties of waste electric porcelain solar absorption and thermal storage integrated ceramics (SATS ceramics) were investigated in depth, and the following conclusions were drawn:

(1) At a sintering temperature of 1400 °C and a magnetite content of 11 wt.%, the material formed an optimal short-cluster, ordered interwoven columnar mullite structure, resulting in a flexural strength of 96.05 MPa and a bulk density of 2.35 g/cm^3, which significantly enhanced the material's properties.

(2) Thermophysical analyses showed that the specific heat capacity (Cp) of the ceramics increased with increasing temperature, and that sample BK4 had the highest Cp value of 0.6415 J/(g* °C) at 300 °C, indicating excellent thermophysical properties.

(3) XRD and SEM analyses confirmed the massive formation of mullite phase and grain growth under the optimized conditions, while physical property tests revealed the trends of porosity, bulk density, and water absorption, which affect the thermal stability and mechanical strength of the materials.

Author Contributions: Resources, Z.L. and X.S.; writing—original draft preparation, X.Z., X.W. and X.C.; writing—review and editing, Z.L. and X.S.; visualization, J.W., M.F., F.F. and S.S.; supervision, Z.L. and X.S.; funding acquisition, Z.L. All authors have read and agreed to the published version of the manuscript.

Funding: This research was funded by Scientific Research Foundation for High-level Talents of Anhui University of Science and Technology (2021yjrc49), Anhui International Joint Research Center for Nano Carbon-based Materials and Environmental Health (NCMEH2024Y01), Anhui Provincial Natural Science Foundation (2208085QE171), the University Synergy Innovation Program of Anhui Province (GXXT-2023-019, GXXT-2022-083), National Natural Science Foundation of China (NSFC) (52227901), Graduate Innovation Fund of Anhui University of Science and Technology (2024cx2090), Innovation and Entrepreneurship Training Program for Undergraduates (202310361017, 202410361017).

Data Availability Statement: All data included in this study are available upon request by contact with the corresponding author.

Acknowledgments: This present work was supported by Analytical and testing center (Anhui University of Science and Technology) and Key Laboratory of Industrial Dust Prevention and Control & Occupational Health and Safety (Ministry of Education, Anhui University of Science and Technology).

Conflicts of Interest: The authors declare no conflicts of interest.

References

1. Cao, Y.; Lv, Z.; Zhang, K.; Lan, C.; Fan, M.; Lu, X. Waste electric porcelain-based refractory bricks with significantly enhanced mechanical properties: Preparation, characterization and mechanism. *Ceram. Int.* **2024**, *50*, 49698–49711. [CrossRef]
2. Qiu, Z.; Sun, Y.; Cui, Y.; Zhang, Z.; Liu, Y.; Chen, X. Optimized Design of Shed Parameters for Polluted Hollow Porcelain Insulators at High Altitude. *IEEE Access* **2023**, *11*, 63451–63462. [CrossRef]
3. Lv, Z.; Cao, Y.; Lan, C.; Fan, M.; Ke, Y.; Guo, W.; Yang, Y. Property dependence on particle size and sintering temperature of waste porcelain high-temperature resistant material. *Int. J. Appl. Ceram. Technol.* **2025**, *22*, e14890. [CrossRef]
4. Dai, S.; Li, M.; Wu, X.; Wu, Y.; Li, X.; Hao, Y.; Luo, B. Combinatorial optimization of perovskite-based ferroelectric ceramics for energy storage applications. *J. Adv. Ceram.* **2024**, *13*, 877–910. [CrossRef]
5. Chu, S.; Majumdar, A. Opportunities and challenges for a sustainable energy future. *Nature* **2012**, *488*, 294–303. [CrossRef] [PubMed]
6. Keshavarz, Z.; Mostofinejad, D. Effects of high-temperature exposure on concrete containing waste porcelain coarse aggregates and steel chips. *J. Build. Eng.* **2020**, *29*, 101211. [CrossRef]
7. Gautam, L.; Kalla, P.; Jain, J.K.; Choudhary, R.; Jain, A. Robustness of self-compacting concrete incorporating bone china ceramic waste powder along with granite cutting waste for sustainable development. *J. Clean. Prod.* **2022**, *367*, 132969. [CrossRef]
8. Shen, X.; Zhu, L.; Lv, Z.; Shi, T.; Yin, Z.; Min, X. The Behavior of Slag Resistance of MgO-C Refractory Prepared by Sucrose as Binder. *IOP Conf. Ser. Mater. Sci. Eng.* **2019**, *678*, 012091. [CrossRef]
9. Wang, R.; Liu, X.; Wei, H.; Xu, Y.; Zhou, R.; Huang, Z.; Zhan, H. Study on phase behavior and mechanical properties of high temperature resistant materials prepared from waste electric porcelain. *Ceram. Int.* **2023**, *49*, 11537–11543. [CrossRef]
10. Pivák, A.; Pavlíková, M.; Záleská, M.; Lojka, M.; Lauermannová, A.-M.; Jankovský, O.; Pavlík, Z. Low-Carbon Composite Based on MOC, Silica Sand and Ground Porcelain Insulator Waste. *Processes* **2020**, *8*, 829. [CrossRef]
11. López-Perales, J.F.; Sánchez-Rodríguez, R.; Suárez-Suárez, D.D.; Rodríguez, E.A. Fired electrical porcelain scrap (chamotte waste) recycling and reuse as an alternative raw material for sustainable porcelain stoneware production. *J. Clean. Prod.* **2024**, *434*, 140385. [CrossRef]
12. Talaei, M.; Mostofinejad, D. Mechanical properties of fiber-reinforced concrete containing waste porcelain aggregates under elevated temperatures. *Constr. Build. Mater.* **2021**, *289*, 122854. [CrossRef]
13. Xu, X.; Shen, Y.; Wu, J.; Zhang, Z.; Yu, J.; Qiu, S. The thermal shock resistance of in-situ synthesized mullite absorption and storage integrated ceramics for solar thermal power generation. *Ceram. Int.* **2024**, *50*, 7843–7852. [CrossRef]
14. Xu, X.; Song, J.; Wu, J.; Zhang, Y.; Zhou, Y.; Zhang, Q. Preparation and Thermal Shock Resistance of Mullite and Corundum Co-bonded SiC Ceramics for Solar Thermal Storage. *J. Wuhan Univ. Technol.-Mater. Sci. Ed.* **2020**, *35*, 16–25. [CrossRef]
15. Xu, X.; Liu, S.; Liu, Y.; Wu, J.; Yu, J.; Shen, Y. Preparation and thermal shock resistance of solar thermal absorbing corundum ceramics for concentrated solar power. *Int. J. Appl. Ceram. Technol.* **2024**, *21*, 2102–2113. [CrossRef]
16. Chen, Y.; Zhou, Z.; Li, L.; Wu, D.; Wang, Q. Synergistically enhancing the piezoelectric activity and Curie temperature of $CaBi_4Ti_4O_{15}$ ceramics via co-doping Gd/Mn at the A/B-site. *J. Adv. Ceram.* **2024**, *13*, 1482–1497. [CrossRef]
17. Yang, Y.; Hu, C.; Liu, Q.; Li, J. Research progress and prospects of colored zirconia ceramics: A review. *J. Adv. Ceram.* **2024**, *13*, 1505–1522. [CrossRef]
18. Huan, Y.; Gui, D.; Li, C.; Wei, T.; Wu, L. Simultaneously enhanced energy storage performance and luminance resistance in $(K_{0.5}Na_{0.5})$ NbO_3-based ceramics via synergistic optimization strategy. *J. Adv. Ceram.* **2024**, *13*, 34–43. [CrossRef]

19. Ning, Y.; Pu, Y.; Wu, C.; Chen, Z.; Zhang, X.; Zhang, L.; Wang, B. Design strategy of high-entropy perovskite energy-storage ceramics: A review. *J. Eur. Ceram. Soc.* **2024**, *44*, 4831–4843. [CrossRef]
20. Xu, X.; Shen, Y.; Zhang, Z.; Wu, J.; Yu, J.; Zhou, Y. Influence of Fe_2O_3 on the absorptivity of in situ synthesized solar high-temperature absorbing and storing integrated mullite-based ceramics. *Ceram. Int.* **2024**, *50*, 27339–27348. [CrossRef]
21. Lao, X.; Xu, X.; Wu, J.; Xu, X. High-temperature alloy/honeycomb ceramic composite materials for solar thermal storage applications: Preparation and stability evaluation. *Ceram. Int.* **2017**, *43*, 4583–4593. [CrossRef]
22. Hu, C.; Wu, J.; Xu, X.; Chen, P. Investigating the effect of andalusite on mechanical strength and thermal shock resistance of cordierite-spodumene composite ceramics. *Ceram. Int.* **2018**, *44*, 3240–3247. [CrossRef]
23. Xu, X.; Wang, Y.; Wu, J.; Liu, S.; Ma, S.; Cheng, T. Preparation and characterization of solar absorption and thermal storage integrated ceramics from calcium and iron-rich steel slag. *Ceram. Int.* **2023**, *49*, 8381–8389. [CrossRef]
24. Xu, X.; Li, M.; Wang, Y.; Wu, J.; Liu, S.; Ma, S.; Cheng, T. Preparation and thermal shock resistance of solar thermal storage ceramics from high calcium and high iron steel slag. *Ceram. Int.* **2024**, *50*, 8099–8108. [CrossRef]
25. Xu, X.; Li, J.; Wu, J.; Tang, Z.; Li, Y.; Lu, C. Preparation and thermal shock resistance of corundum-mullite composite ceramics from andalusite. *Ceram. Int.* **2017**, *43*, 1762–1767. [CrossRef]
26. Lao, X.; Xu, X.; Cheng, H.; Liu, H.; Liang, L. Effect of rare-earth oxides on microstructure and thermal shock resistance of Al_2O_3-SiCw composite ceramics for solar thermal storage. *Ceram. Int.* **2019**, *45*, 2003–2011. [CrossRef]
27. Liu, Y.; Xu, Y.; Zhou, R.; Wei, H.; Zhang, W.; Zhan, H.; Ma, S.; Yang, C.; Huang, Z. Study on Preparation of Porous Light Refractory from Waste Electric Porcelain. *ChemistrySelect* **2024**, *9*, e202303743. [CrossRef]
28. Gautam, L.; Kumar Jain, J.; Jain, A.; Kalla, P. Valorization of bone-china ceramic powder waste along with granite waste in self-compacting concrete. *Constr. Build. Mater.* **2022**, *315*, 125730. [CrossRef]
29. Wu, J.; Hao, S.; Xu, X.; Ma, S.; Li, P.; Shi, X. Preparation of $MgAl_2O_4$ solar thermal storage ceramics from different magnesium sources. *Int. J. Appl. Ceram. Technol.* **2023**, *20*, 3223–3236. [CrossRef]
30. Zhang, L.; Pu, Y.; Chen, M.; Peng, X.; Wang, B.; Shang, J. Design strategies of perovskite energy-storage dielectrics for next-generation capacitors. *J. Eur. Ceram. Soc.* **2023**, *43*, 5713–5747. [CrossRef]
31. Liang, Z.; Wang, Y.; Zhu, Q. Multi-mode luminescent ceramic glaze for advanced anti-counterfeiting. *Opt. Mater.* **2024**, *157*, 116152. [CrossRef]
32. Almeida, C.M.R.; Ghica, M.E.; Durães, L. An overview on alumina-silica-based aerogels. *Adv. Colloid Interface Sci.* **2020**, *282*, 102189. [CrossRef]
33. Zou, J.; Zhang, G.J.; Kan, Y.M. Pressureless densification and mechanical properties of hafnium diboride doped with B_4C: From solid state sintering to liquid phase sintering. *J. Eur. Ceram. Soc.* **2010**, *30*, 2699–2705. [CrossRef]
34. Vassilev, S.V.; Vassileva, C.G. A new approach for the classification of coal fly ashes based on their origin, composition, properties, and behaviour. *Fuel* **2007**, *86*, 1490–1512. [CrossRef]
35. Elsayed, A.H.; Sayed, M.A.; Dawood, O.M.; Daoush, W.M. Effect of Transition Metals Oxides on the Physical and Mechanical Properties of Sintered Tungsten Heavy Alloys. *Crystals* **2020**, *10*, 825. [CrossRef]
36. Jia, J.; Wu, D.; Ren, Y.; Lin, J. Nanoarchitectonics of Illite-Based Materials: Effect of Metal Oxides Intercalation on the Mechanical Properties. *Nanomaterials* **2022**, *12*, 997. [CrossRef]
37. Hou, Z.; Cui, B.; Liu, L.; Liu, Q. Effect of the different additives on the fabrication of porous kaolin-based mullite ceramics. *Ceram. Int.* **2016**, *42*, 17254–17258. [CrossRef]
38. Feng, M.; Wu, Y.-Q.; Ji, G.-R.; Zhou, Y.; Wang, X.-J. Sintering mechanism and properties of corundum-mullite duplex ceramic with MnO_2 addition. *Ceram. Int.* **2022**, *48*, 14237–14245. [CrossRef]
39. Lv, Z.; Lan, C.; Cao, Y.; Fan, M.; Ke, Y.; Guo, W.; Yang, Y.; Shen, X. One-step preparation of N-doped porous carbon materials with excellent microwave absorption properties based on methylene blue saturated wood-based activated carbon. *Carbon Lett.* **2024**. [CrossRef]
40. Shen, X.; Lv, Z.; Ichikawa, K.; Sun, H.; Huang, Z.; Koide, S.; Liao, M. Stress effect on the resonance properties of single-crystal diamond cantilever resonators for microscopy applications. *Ultramicroscopy* **2022**, *234*, 113464. [CrossRef]
41. Alves, M.F.R.P.; Ribeiro, S.; Suzuki, P.A.; Strecker, K.; Santos, C.D. Effect of Fe_2O_3 Addition and Sintering Temperature on mechanical Properties and Translucence of Zirconia Dental Ceramics with Different Y_2O_3 Content. *Mater. Res.* **2021**, *24*, e20200402. [CrossRef]
42. Hu, Z.; Liu, Z.; Han, B.; Peng, H.; Dai, K.; Xu, Z.; Fu, Z.; Hu, Z.; Wang, G. Designing silver niobate-based relaxor antiferroelectrics for ultrahigh energy storage performance. *J. Adv. Ceram.* **2024**, *13*, 1282–1290. [CrossRef]
43. Tian, Y.; Xue, F.; Li, L.; Qiu, L.; Xie, Y.; Du, G. High energy storage performance of $Bi_{0.5}Na_{0.5}TiO_3$-$Ba_{0.65}Sr_{0.35}TiO_3$-$AgNbO_3$ relaxor ferroelectrics with excellent temperature and frequency stability. *Mater. Sci. Eng. B-Adv. Funct. Solid-State Mater.* **2024**, *309*, 117600. [CrossRef]
44. Xiong, X.; Liu, H.; Zhang, J.; Da Silva, L.L.; Sheng, Z.; Yao, Y.; Wang, G.; Hinterstein, M.; Zhang, S.; Chen, J. Ultrahigh Energy-Storage in Dual-Phase Relaxor Ferroelectric Ceramics. *Adv. Mater.* **2024**, *36*, 2410088. [CrossRef] [PubMed]

45. Lv, Z.; Liu, H.; Zhang, X.; Shen, X.; Liu, S.; Wu, X.; Fang, M.; Liu, Y.; Min, X.; Huang, Z. Solvothermally synthesized highly porous $W_{18}O_{49}$ nanowires for UV, humidity and pH detection. *Phys. E: Low-Dimens. Syst. Nanostructures* **2020**, *117*, 113719. [CrossRef]
46. Wu, J.; Zhang, Z.; Xu, X.; Ma, S.; Li, P.; Shi, X. Preparation and Thermal Shock Resistance of Mullite Ceramics for High Temperature Solar Thermal Storage. *J. Wuhan Univ. Technol.-Mater. Sci. Ed.* **2023**, *38*, 743–752. [CrossRef]
47. Wu, J.; Yu, J.; Xu, X.; Liu, Y.; Zhang, Z.; Wei, P. Preparation and thermal shock resistance of anorthite solar thermal energy storage ceramics from magnesium slag. *Ceram. Int.* **2022**, *48*, 33604–33614. [CrossRef]